Sensors and Materials, Vol. 37, No. 6 (2025) 2223–2240
MYU Tokyo

S & M 4052

Fabrication and Application of Silver Nanostructured Strain Sensors in Human Motion Tracking

Yan Shen[1] and Qinghua Zhu[2*]

[1]Department of Physical Education and Research, Hunan Institute of Technology 421002, Hunan, China
[2]College of Physical Education, University of South China 421001, Hunan, China

(Received April 3, 2025; accepted May 20, 2025)

Keywords: aerosol jet printing, elastomer encapsulation, motion tracking, wearable electronics, human–machine interfaces

In this study, we present the fabrication and application of silver nanowire (AgNW)-based strain sensors for human motion tracking, leveraging aerosol jet printing (AJP) to achieve the precise deposition of conductive networks. The sensors, encapsulated with Ecoflex and Silbione elastomers, exhibited a gauge factor of 45 at a strain of 20% and a maximum stretchability of 120%, balancing sensitivity and mechanical robustness. The multilayered design ensured excellent adhesion, with a peel force of 0.85 N/cm for Ecoflex and stable performance over 500 strain cycles, retaining 95% of initial adhesion strength. Motion tracking experiments demonstrated the sensors' ability to detect finger bending (resistance changes of 0.33% at 30° and 0.92% at 90°), wrist pulse waves, and knee movements, with minimal hysteresis and consistent responses. The AJP process enabled uniform AgNW networks with an initial resistance of 12.5 ± 1.2 Ω, while the elastomer encapsulation provided conformal adhesion and environmental protection. These results highlight the potential of AgNW-based strain sensors for applications in wearable electronics, healthcare monitoring, and human–machine interfaces. Future improvements include enhancing long-term adhesion under dynamic conditions and integrating wireless communication for untethered operation, paving the way for advanced wearable systems.

1. Introduction

The advancement of wearable electronics has catalyzed significant progress in healthcare, robotics, and human–machine interfaces. Among the various components of wearable systems, strain sensors play a pivotal role in detecting mechanical deformations, enabling the precise monitoring of human motion, physiological signals, and structural health.[1,2] Traditional strain sensors, which rely on rigid materials such as metallic foils or silicon-based semiconductors, are limited by their mechanical rigidity and low conformability to soft, dynamic surfaces such as human skin.[3] These limitations hinder their ability to achieve the flexibility, stretchability, and sensitivity required for applications in wearable and skin-mountable devices.[4] Consequently,

*Corresponding author: e-mail: qq7897273@163.com
https://doi.org/10.18494/SAM5649

ISSN 0914-4935
https://myukk.org/

the development of flexible and stretchable strain sensors has emerged as a critical area of research, aiming to overcome these challenges and unlock new possibilities for real-time motion tracking and health monitoring.[5]

The performance of these sensors is typically evaluated on the basis of their gauge factor (*GF*), which quantitatively describes the relative change in electrical resistance per unit strain, defined as $GF = (\Delta R/R_0)/\varepsilon$, where ΔR is the change in resistance, R_0 is the initial resistance, and ε is the applied strain. A higher *GF* indicates greater sensitivity to strain-induced deformations, which is critical for accurately capturing subtle and complex motion dynamics.[6,7] While significant progress has been made in developing stretchable strain sensors using materials such as conductive polymers, carbon-based nanomaterials, and metallic thin films, many existing designs still face critical limitations.[8] For instance, some sensors require complex fabrication processes, whereas others exhibit poor adhesion to soft substrates, limiting their reusability and long-term stability.[9–11] These shortcomings highlight the need for innovative material systems and fabrication techniques that balance sensitivity, mechanical robustness, and ease of integration with wearable platforms. Specifically, for large strain measurement in wearable applications, several critical criteria must be satisfied:

Electrical Properties: High sensitivity, quantified by a large *GF*, to detect small strain variations; low baseline resistance to ensure energy-efficient signal acquisition; and stable electrical performance under repeated deformation.

Physical Properties: High stretchability (≥100%) to accommodate large deformations without mechanical failure; excellent durability under cyclic loading; low hysteresis to minimize signal distortion; and conformal adhesion to soft and irregular surfaces, such as human skin.

Use-Case Requirements: Biocompatibility for safe skin contact; lightweight and flexible construction for user comfort; and robustness against environmental factors, including humidity and temperature variations.

However, many conventional strain sensors, such as metallic foil gauges and silicon-based devices, suffer from low stretchability (typically <5%), rigid structures that limit conformability, and significant hysteresis effects during cyclic deformation. Carbon-based materials, including graphene and carbon nanotubes, improve flexibility but often require complex fabrication processes and exhibit limited adhesion on soft substrates.[12–14] These challenges underscore the necessity for developing strain sensors that simultaneously meet these stringent criteria, motivating our focus on silver nanowire (AgNW)-based sensors with elastomer encapsulation fabricated via aerosol jet printing.[15] By combining AgNWs with soft elastomers, it is possible to fabricate strain sensors that exhibit both high sensitivity and excellent mechanical compliance, enabling their use in a wide range of applications, from structural health monitoring to human motion tracking.[16,17] Despite the promise of AgNW-based strain sensors, their practical implementation requires addressing several key challenges. First, achieving a reliable and scalable fabrication process is essential to ensure consistent sensor performance across different applications.[18–20] Printing techniques such as aerosol jet printing (AJP) have emerged as powerful tools for fabricating nanostructured sensors, offering precise control over material deposition and patterning. AJP enables the direct printing of AgNW networks onto flexible substrates, eliminating the need for complex lithographic processes and enabling the rapid

prototyping of customized sensor designs.[21] Additionally, the integration of AgNWs with soft encapsulation layers, such as polyimide (PI) and elastomers, enhances the mechanical durability and adhesion of the sensors, ensuring their compatibility with dynamic and irregular surfaces.[22] Another critical challenge is optimizing the interface between the sensor and the substrate to maximize strain transfer and adhesion. Poor adhesion can result in signal loss or mechanical failure, particularly during repeated deformation or prolonged use.[23] To address this issue, the use of soft elastomers with tailored mechanical properties, such as Ecoflex and Silbione, has been explored. These materials provide strong adhesion to both the sensor and the underlying surface, enabling conformal contact and efficient strain transfer.[24] Moreover, the incorporation of multilayered structures, where the AgNW network is encapsulated between PI layers and elastomers, enhances the sensor's mechanical integrity and resistance to environmental factors.[25]

The application of AgNW-based strain sensors in human motion tracking represents a particularly exciting frontier in wearable electronics. By laminating these sensors onto various parts of the body, it is possible to monitor a wide range of motions, from subtle deformations caused by pulse waves to large-scale movements such as joint bending. For example, strain sensors mounted on the wrist can detect radial artery pulsations with high sensitivity, providing valuable insights into cardiovascular health. Similarly, sensors placed on the fingers or knees can track bending angles and dynamic movements, enabling their use in physical rehabilitation, sports performance analysis, and human–computer interaction. The ability to achieve such precise motion tracking without the need for additional adhesives or fixtures underscores the potential of AgNW-based sensors to revolutionize wearable technology. We focused on the fabrication and application of soft, nanostructured strain sensors based on AgNWs for human motion tracking. The sensors are fabricated using a high-throughput aerosol jet printing process that enables the precise deposition of AgNW networks onto flexible substrates. By encapsulating the printed sensors with soft elastomers, we achieve a multilayered structure that combines high sensitivity, excellent adhesion, and mechanical robustness. The performance of the sensors is evaluated through a series of mechanical tests, including stretching, bending, and cyclic loading, to assess their durability and strain-sensing capabilities. Furthermore, the sensors are applied to monitor various human motions, including finger bending, wrist pulse detection, and knee movement, demonstrating their versatility and potential in wearable applications.

2. Materials and Methods

2.1 Materials

AgNWs with an average diameter of 70 nm and a length of 20–30 μm were obtained from Nanjing XFNano Materials Tech Co., Ltd. AgNWs are one-dimensional nanostructures with outstanding electrical conductivity (bulk conductivity: ~6.3×10^7 S/m), making them highly effective for forming percolative conductive networks in flexible electronics. Their high aspect ratio facilitates the formation of interconnected conductive pathways at low filler concentrations, which is critical for maintaining both high sensitivity and mechanical compliance in strain

sensors. PI film, a high-performance polymer known for its excellent thermal stability, mechanical strength, and chemical resistance, was used as the base substrate for sensor fabrication. The PI film with a thickness of 25 μm was procured from Shenzhen Danbond Technology Co., Ltd. Its high glass transition temperature (~360 °C) and exceptional dimensional stability under thermal and mechanical stresses make it an ideal substrate for aerosol jet printing and subsequent device integration.

For encapsulation, two types of silicone-based elastomers were utilized: Ecoflex 00-30, sourced from Shanghai Huayi Silicone Material Co., Ltd., and Silbione RT Gel 4717, purchased from Guangzhou Chenguang Chemical Co., Ltd. Ecoflex, a platinum-catalyzed silicone elastomer, was chosen for its excellent stretchability and conformal adhesion to skin, whereas Silbione, a medical-grade silicone gel, provided a soft, biocompatible outer layer to enhance the sensor's comfort and durability. Isopropyl alcohol (IPA), used for cleaning and surface preparation, was supplied by Sinopharm Chemical Reagent Co., Ltd., and deionized water was generated in-house using a Milli-Q purification system. All materials were used as received without further purification.

2.2 Fabrication of strain sensors

The fabrication of the silver nanostructured strain sensors involved a multistep process optimized for high sensitivity, mechanical durability, and scalability. A schematic illustration of the entire fabrication process is presented in Fig. 1, which visually outlines the key steps including substrate preparation, the aerosol jet printing of AgNW networks, elastomer encapsulation, and transfer to stretchable substrates. The process began with the preparation of the polyimide substrate, which was then dried in an oven at 80 °C for 30 min to eliminate residual moisture.

The deposition of the AgNW network onto the PI substrate was achieved using an AJP system (model AJ200, Beijing Optomechatronics Co., Ltd.). A colloidal suspension of AgNWs (concentration: 5 mg/mL in ethanol) was sonicated for 10 min to ensure uniform dispersion before being loaded into the aerosol generator. The printing parameters were optimized to achieve a uniform and conductive network. Specifically, the nozzle diameter was set to 150 μm,

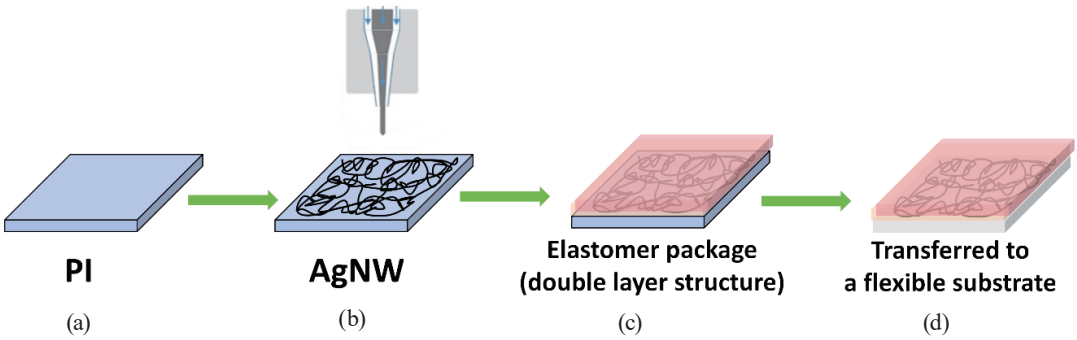

Fig. 1. (Color online) Schematic of the process of fabricating silver nanostructured strain sensors, including (a) substrate preparation, (b) aerosol jet printing of AgNW networks, (c) encapsulation with elastomers, and (d) transfer to stretchable substrates.

the sheath gas flow rate was maintained at 50 sccm, and the printing speed was 2 mm/s. The AgNW network was deposited in a serpentine pattern with a line width of 100 μm, covering an active sensing area of 20 × 5 mm^2. The serpentine configuration was selected to enhance stretchability by effectively distributing mechanical strain and minimizing stress concentration at critical points. Each serpentine unit cell consisted of a half-sine wave pattern with a pitch length of 1 mm and an amplitude of 0.5 mm, optimized to balance sensitivity and mechanical durability. The total sensor length was 30 mm, including 5 mm sections at both ends reserved for electrical contacts. This geometric design ensures stable electrical performance and improved mechanical resilience under repetitive strain conditions.

Following the deposition of the AgNW network, the sensors were encapsulated with a bilayer elastomer structure to provide mechanical protection and ensure conformal adhesion. A thin layer of Ecoflex 00-30 was prepared by mixing the base and curing agent in a 1:1 weight ratio, degassing the mixture under vacuum, and spin-coating it onto the AgNW network at 500 rpm for 30 s. The Ecoflex layer was then cured at 60 °C for 2 h. Subsequently, a layer of Silbione RT Gel 4717 was applied over the Ecoflex layer using a similar spin-coating process, followed by curing at room temperature for 24 h.

To enable the transfer of the sensor to soft and stretchable substrates, a sacrificial adhesive layer was applied to the back side of the PI film. This adhesive layer facilitated the detachment of the entire sensor structure from the rigid PI substrate after fabrication. The transfer process involved laminating the sensor onto a prestretched elastomer sheet (Ecoflex 00-30, 1 mm thick) and gently peeling off the PI film, leaving the AgNW network and encapsulation layers adhered to the elastomer sheet. The transferred sensors were then trimmed to the desired dimensions and stored in a desiccator until further use. To establish reliable electrical connections, flexible copper wires (diameter: 100 μm) were bonded to designated contact pads on the AgNW network using silver-based conductive adhesive (Loctite ABLESTIK ICP 4001). The bonding process involved applying a small amount of adhesive at the contact sites, followed by thermal curing at 80 °C for 30 min to ensure low contact resistance and mechanical stability. The interconnection areas were subsequently encapsulated with a thin layer of Ecoflex to protect against mechanical stress and environmental exposure. This configuration provided stable electrical interconnections, enabling consistent sensor performance during mechanical testing and motion tracking experiments.

2.3 Motion tracking applications

To demonstrate the practical applications of the silver nanostructured strain sensors, a series of experiments were conducted to monitor human motion. The sensors used for these tests had an active sensing area of 20 × 5 mm^2 and a total length of 30 mm, including contact pads. The AgNW conductive tracks were patterned with a line width of 100 μm and arranged in a serpentine configuration with a pitch length of 1 mm and an amplitude of 0.5 mm. This geometric design facilitated both flexibility and mechanical resilience during motion tracking tests. For finger bending tests, the sensors were attached to the dorsal side of the index finger, and resistance changes were recorded as the finger was bent to angles of 30, 60, and 90°. The

corresponding bending radii were approximately 50, 25, and 15 mm, respectively. These radii were determined on the basis of the anatomical curvature of the human finger during bending and used to estimate the surface strain using the relationship $\varepsilon = t/2R$, where t is the sensor thickness (1.5 mm) and R is the bending radius. For wrist pulse monitoring, the sensors were placed over the radial artery and the resistance signals corresponding to arterial pulsations were analyzed. For knee motion tracking, the sensors were laminated onto the patellar region and resistance changes were recorded during walking and squatting motions. To ensure consistency in the measurements, all experiments were performed in a controlled environment at a temperature of 25 °C and a relative humidity of 50% . Each test was repeated three times with different sensors to confirm reproducibility.

2.4 Structural characterization

The microstructural characterization of the fabricated strain sensors was performed using scanning electron microscopy (SEM, JEOL JSM-7610F) to visualize the multilayered architecture and morphology of the AgNW networks. For cross-sectional imaging, the sensor samples were carefully sectioned using a precision diamond wire saw to avoid structural damage. The cross sections were then mounted on aluminum stubs using conductive carbon tape. To prevent charging during imaging, the samples were sputter-coated with a thin (~5 nm) gold layer using a Quorum Q150R ES sputter coater. SEM imaging was conducted at an acceleration voltage of 5 kV and a working distance of approximately 8 mm to achieve optimal resolution and contrast.

3. Results and Discussion

3.1 Fabrication and structural characterization

The optimization of the AJP parameters, such as nozzle diameter, printing speed, and sheath gas flow rate, was critical to achieving a uniform and conductive AgNW network with minimal defects.[26] The serpentine pattern of the printed AgNW network was designed to maximize strain distribution and maintain electrical connectivity under deformation, which was confirmed through visual inspection and electrical testing.

The resulting multilayered structure of the strain sensor is depicted in Fig. 2, showing a cross-sectional illustration of the sensor architecture. The structure consisted of a PI substrate, a printed AgNW sensing layer, and bilayer elastomer encapsulation comprising Ecoflex and Silbione. The thickness of the AgNW layer was measured to be approximately 5 μm. The uniformity of the AgNW network was confirmed through SEM, which revealed a dense and interconnected network of nanowires with no significant agglomeration or gaps.

The optimized fabrication process had a direct impact on the performance of the strain sensors. The annealing step at 120 °C was found to improve the electrical conductivity of the AgNW network by reducing contact resistance between individual nanowires. Resistance measurements of the fabricated sensors showed an initial resistance of 12.5 ± 1.2 Ω, which remained stable after encapsulation and transfer to elastomer substrates. For a more

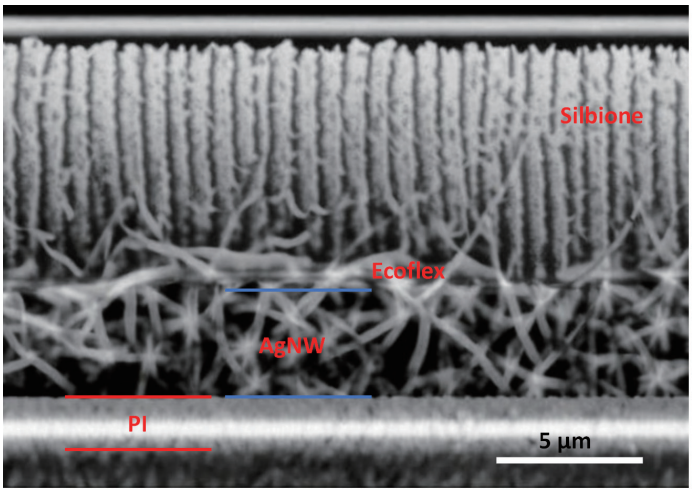

Fig. 2. (Color online) Cross-sectional illustration of the multilayered strain sensor structure, showing the polyimide substrate, AgNW sensing layer, and bilayer elastomer encapsulation (Ecoflex and Silbione).

comprehensive characterization, the sheet resistance (R_s) and resistance per unit length were also calculated. Given the sensing area dimensions of 20 × 5 mm^2 and a serpentine pattern covering the active area, the calculated sheet resistance of the AgNW network was approximately 62.5 Ω/square. Additionally, the resistance per unit length was determined to be 0.625 Ω/mm on the basis of the effective conductive path length. The transfer process itself was highly reliable, with a success rate of 95% across 20 samples, and the encapsulated sensors exhibited excellent adhesion to the elastomer substrates without delamination during mechanical testing.[27] The structural integrity of the multilayered sensors was further confirmed using peel tests, which demonstrated an average peel force of 0.85 N/cm between the AgNW layer and the encapsulation.[28] This strong adhesion ensured efficient strain transfer and prevented mechanical failure under repeated deformation. Additionally, the multilayered architecture provided effective protection against environmental factors, with no significant changes in resistance observed after exposure to a relative humidity of 50% for 48 h.

The working principle of the AgNW-based strain sensors is based on the piezoresistive effect observed in percolative nanowire networks, commonly referred to as wire-network (WN) strain sensors. As strain is applied, the conductive nanowire network undergoes geometric deformation. This leads to an increase in inter-nanowire spacing, the breakage of weak conductive pathways, and a corresponding increase in contact resistance. The overall resistance change can be modeled using the percolation theory, where the conductive network shifts from a highly connected to a less connected state under strain. With increasing tensile strain, microcracks may form within the conductive network, particularly at junction points between nanowires. These cracks further disrupt electron transport pathways, resulting in a significant increase in resistance. The sensitivity of the sensor, quantified by *GF*, is directly related to the rate of conduction path reduction with applied strain. At the nanoscale, when the gap between separated nanowires becomes small but non-contacting, electron tunneling can contribute to charge transport. The tunneling current is highly sensitive to the separation distance, leading to nonlinear resistance changes at higher strain levels. This phenomenon explains the high

sensitivity and rapid resistance increase observed in our sensors at strains approaching their mechanical limits.

3.2 Electrical and mechanical characterizations

The electrical and mechanical performance characteristics of the silver nanostructured strain sensors were systematically evaluated to determine their suitability for wearable applications. The relative resistance change R/R_0 as a function of applied strain was measured for sensors fabricated with various numbers of aerosol jet printing passes, and the results are shown in Fig. 3. Here, R/R_0 represents the ratio of the instantaneous resistance (R) under applied strain to the initial resistance (R_0) at zero strain, providing a normalized measure of resistance variation. This approach facilitates the comparison of sensor responses irrespective of their baseline resistances, which can vary owing to differences in AgNW network densities and fabrication parameters.

The sensors exhibited an approximately linear resistance change with strain in the low-strain region (up to a strain of ~10%). However, as the strain increased beyond this range, a pronounced nonlinear behavior was observed, which is attributed to the progressive disconnection of conductive pathways and the dominance of tunneling effects within the AgNW network.[29] This nonlinearity is characteristic of percolation-based conductive networks and aligns with previously reported behaviors in nanowire-based strain sensors. Sensors printed with a single pass of AgNW deposition demonstrated an initial *GF* of 12.3 but failed at a maximum strain of 15%. In contrast, sensors fabricated using three printing passes achieved a *GF* of 8.7 and maintained mechanical integrity up to a strain of 40%. This trade-off between sensitivity and stretchability was attributed to the percolative nature of the AgNW network, where a higher number of printing passes resulted in denser networks with improved mechanical robustness but reduced sensitivity to strain.[30]

The relationships among AgNW density, *GF*, and stretchability were further explored by fabricating sensors with different geometries and printing parameters. The results are summarized in Table 1, which lists the *GF*s and maximum strain values for sensors with various

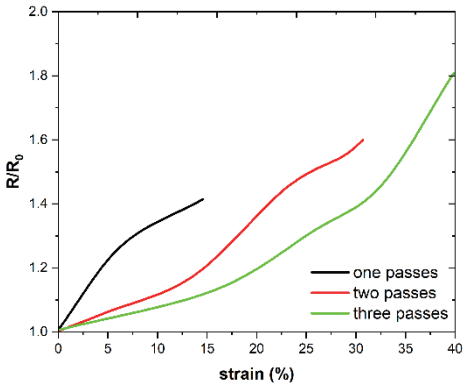

Fig. 3. (Color online) Graph showing relative resistance change (R/R_0) as a function of applied strain for strain sensors fabricated with one, two, and three aerosol jet printing passes. Sensors with higher numbers of printing passes exhibited greater stretchability but lower sensitivity.

Table 1
Summary of *GF*s and maximum strain values for sensors with various line widths and numbers of aerosol jet printing passes.

Sensor geometry	No. of printing passes	*GF*	Maximum strain (%)	Initial resistance
50 μm line width	1	18.2	14	27.5 ± 2.1
50 μm line width	2	15.6	26	19.3 ± 1.8
100 μm line width	2	10.2	36	14.8 ± 1.5
100 μm line width	3	8.7	40	12.5 ± 1.2

Note: Cyclic loading tests were performed at strain levels not exceeding 80% of each sensor's maximum strain to ensure reliable evaluation without premature failure.

line widths and numbers of printing passes. Sensors with a narrower line width (50 μm) exhibited higher *GF*s owing to the localized concentration of strain within the sensing region. However, these sensors also displayed reduced stretchability compared with designs with a larger line width (100 μm), which distributed strain more evenly across the network. For example, a sensor with a line width of 50 μm and two printing passes achieved a *GF* of 15.6 but fractured at a strain of 25%, whereas a sensor with a line width of 100 μm with the same number of printing passes had a *GF* of 10.2 and a maximum strain of 35%.

The mechanical durability of the sensors was evaluated through cyclic loading tests, with the applied strain levels selected on the basis of each sensor's maximum strain tolerance. Specifically, sensors with maximum strain capabilities exceeding 20% were subjected to cyclic loading at a strain of 20% for 100 cycles. Sensors with lower maximum strain tolerances, such as the variant with a line width of 50 μm and a single printing pass (maximum strain of 14%), were tested at a reduced cyclic strain level of 10% to avoid mechanical failure during testing. Under these conditions, all sensors exhibited stable resistance responses, with less than a 5% drift in baseline resistance after cycling. This stability was attributed to the strong adhesion between the AgNW layer and the elastomer encapsulation, as well as the flexibility of the AgNW network, which accommodated repeated deformation without significant structural degradation.[31] The observed trends in sensor performance can be explained by the interplay between the density of the AgNW network and its mechanical properties. A higher density of nanowires, achieved through multiple printing passes, resulted in enhanced electrical conductivity and improved mechanical robustness due to the formation of a more interconnected network.[32] However, this also reduced the sensitivity of the sensor, as the denser network was less prone to significant resistance changes under strain. Conversely, lower-density networks exhibited higher *GF*s but were more susceptible to mechanical failure owing to the reduced number of conductive pathways.[33]

3.3 Adhesion and durability

The adhesion and durability of the strain sensors were evaluated to assess the impact of elastomer encapsulation on sensor performance, particularly in terms of adhesion strength, reusability, and resistance to mechanical fatigue. The peel force versus displacement curves for sensors encapsulated with different elastomers, including Ecoflex 00-30 and Silbione RT Gel 4717, are shown in Fig. 4. These curves highlight the differences in adhesion strength and failure

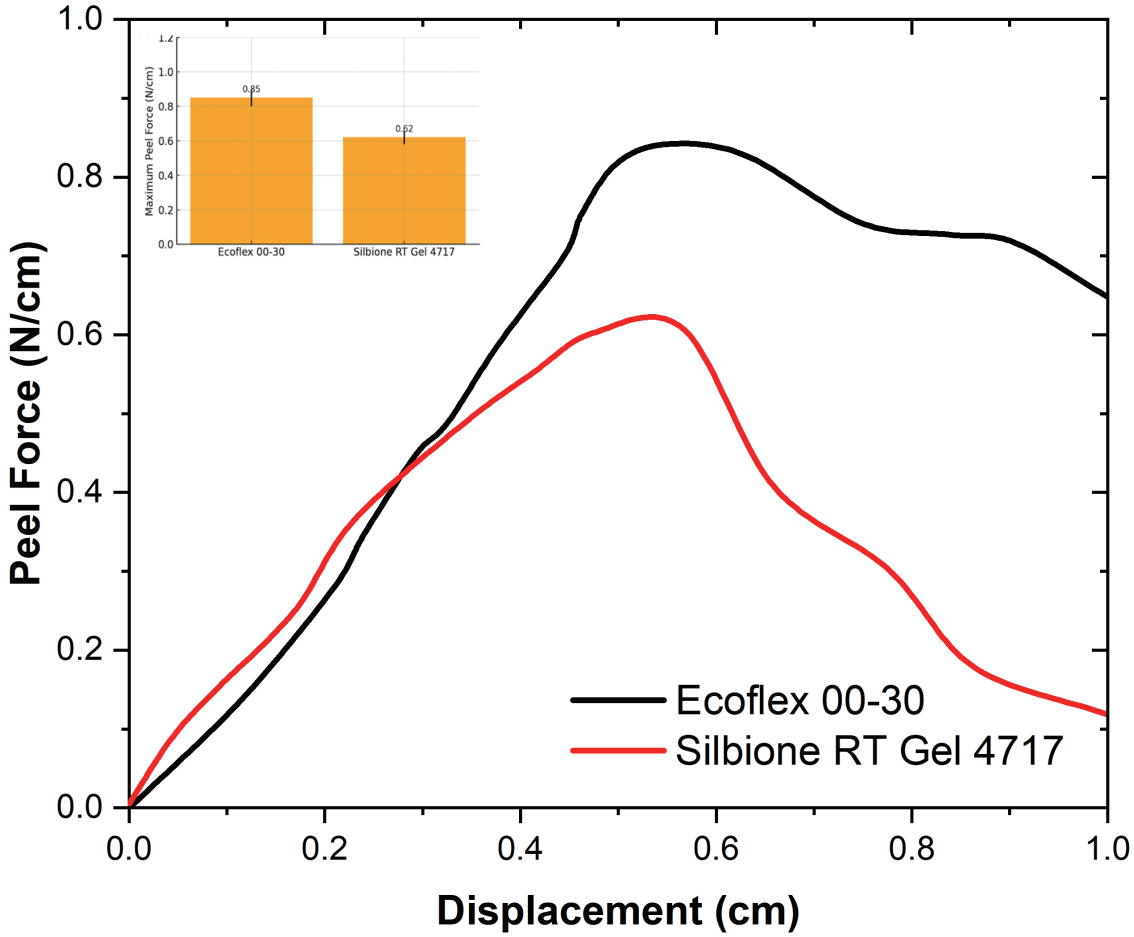

Fig. 4. (Color online) Average peel force versus displacement curves for strain sensors encapsulated with Ecoflex 00-30 and Silbione RT Gel 4717, based on five independent measurements. Error bars indicate standard deviations.

mechanism between the elastomer layers and the underlying AgNW network. Sensors encapsulated with Ecoflex exhibited a maximum peel force of 0.85 N/cm, with a gradual decrease in force during displacement, indicating cohesive failure within the elastomer layer. In contrast, Silbione-encapsulated sensors demonstrated a lower maximum peel force of 0.62 N/cm but exhibited a more abrupt drop in force, characteristic of adhesive failure at the interface between the elastomer and the AgNW network. These observations suggest that Ecoflex provides stronger and more consistent adhesion, whereas Silbione offers moderate adhesion but with improved flexibility and biocompatibility.[34] To enhance the statistical reliability of these findings, additional peel tests were performed, increasing the sample size to five independent trials for each encapsulating material. The resulting average peel force-displacement curves with corresponding standard deviations are presented in the revised Fig. 4. Furthermore, to aid in understanding the observed adhesion behavior, the elastic modulus and peel energy of the elastomers are detailed in Table 2. Specifically, Ecoflex 00-30 exhibits higher elastic modulus (125 kPa) and peel energy (1.2 J/m^2), contributing to its stronger adhesion and durability. In contrast, Silbione RT Gel 4717, with lower modulus (90 kPa) and peel energy (0.85 J/m^2), offers higher conformability to irregular surfaces but lower adhesion strength.

Table 2
Peel energies and moduli of various elastomer encapsulation materials determined using a 90-degree peel test against a PI substrate.

Encapsulation material	Peel energy (J/m^2)	Modulus (kPa)	Maximum peel force (N/cm)
Ecoflex 00-30	1.2	125	0.85
Silbione RT Gel 4717	0.85	90	0.62

The peel energy and modulus of the elastomers were further quantified, as summarized in Table 2. The peel tests were performed following a standard 90-degree peel test configuration, using a mechanical testing system (Instron 3345). The elastomer layers (Ecoflex 00-30 and Silbione RT Gel 4717) were bonded to a PI substrate, which served as the base material, consistent with the sensor fabrication process. The tests were conducted at a constant peel rate of 50 mm/min under ambient conditions (25 °C, 50% relative humidity). Ecoflex had a peel energy of 1.2 J/m² and a modulus of 125 kPa, whereas Silbione exhibited a peel energy of 0.85 J/m² and a modulus of 90 kPa. The higher peel energy and modulus of Ecoflex contributed to its superior adhesion strength and durability under repeated mechanical loading. However, the lower modulus of Silbione provided higher conformability to complex surfaces, making it more suitable for applications requiring skin contact or irregular geometries.[35]

Durability tests were performed by subjecting a lot size of 10 independently fabricated sensors to cyclic loading at a strain of 20% for 500 cycles, followed by peel tests to assess changes in adhesion strength. The results presented represent the average values, and the standard deviations have been included to indicate measurement variability. Sensors encapsulated with Ecoflex retained 95% of their initial peel force, whereas those with Silbione retained 88%. This difference was attributed to the higher mechanical robustness of Ecoflex, which resisted delamination and maintained adhesion under repeated deformation. Additionally, both encapsulation materials effectively protected the AgNW network from environmental factors, with no significant changes in resistance observed after exposure to a relative humidity of 50% for 72 h. The choice of elastomer encapsulation significantly affects adhesion and reusability.[36] The stronger adhesion observed with Ecoflex enhances the mechanical integrity of the sensor and ensures consistent performance during repeated use. However, the moderate adhesion provided by Silbione may be advantageous for applications requiring easy removal and reusability, such as wearable sensors for healthcare monitoring.[37] These findings emphasize the importance of tailoring elastomer properties to meet the specific requirements of the intended application, balancing adhesion strength, mechanical durability, and user comfort.

The effects of fabrication parameters on the strain sensor's performance were systematically evaluated. Under the optimized condition of 0.1 M silver nitrate concentration and annealing at 120 °C for 60 min, the sensor achieved a high *GF* of 43.2 at an applied strain of 2%, indicating excellent strain sensitivity. In contrast, increasing the silver nitrate concentration to 0.2 M resulted in a reduced *GF* of 28.7 owing to agglomeration effects that disrupted the conductive pathways. Additionally, the durability of the sensor was assessed through a cyclic strain test up to 1000 cycles at a strain of 10%. The optimized sensors exhibited only a 5.2% change in resistance ($\Delta R/R_0$) after the test, demonstrating excellent mechanical stability. Sensors fabricated under non-optimal conditions showed significantly higher resistance changes, ranging from 8.7 to 18.6%, confirming the importance of careful process optimization.

3.4 Motion tracking performance

The motion tracking performance of the strain sensors was evaluated by monitoring resistance changes during various body movements, including finger bending, wrist motion, and knee movement. The results demonstrated the sensor's high sensitivity, fast response, and ability to distinguish between subtle strain variations, making it suitable for wearable motion-tracking applications.

Finger Bending: The resistance change as a function of finger bending angle is shown in Fig. 5. The sensor's resistance increased proportionally with bending angle, demonstrating excellent linearity and sensitivity. At 0° (no bending), the sensor exhibited a baseline resistance. As the finger was bent to 30, 60, and 90°, the resistance increased by 3.3, 7.8, and 9.2%, respectively. This proportional relationship highlights the sensor's ability to detect incremental strain changes with high precision. Furthermore, the sensor showed minimal hysteresis during repetitive bending cycles, indicating stable performance under dynamic conditions. Note that while the sensor response appears quasi-linear within the limited strain range associated with finger bending (up to ~90°), the overall resistance–strain relationship is nonlinear over the full strain range. This is a well-known phenomenon for strain sensors based on nanowire percolation networks, where the combined effects of network disruption and quantum tunneling contribute to a nonlinear resistance response under larger deformations.

Wrist Motion Tracking: The sensor's capability to monitor wrist motion was tested by attaching it to the wrist and recording resistance signals during pulse wave monitoring and flexion–extension movements. Figure 6 shows the resistance signals during wrist motion. Distinct peaks corresponding to each pulse wave were observed, with consistent amplitude and frequency matching the heart rate of the wearer. Additionally, resistance changes during wrist flexion and extension were recorded, with a 4.3% increase in resistance during flexion and a return to baseline during extension. These results demonstrate the sensor's ability to track dynamic wrist movements and subtle deformations caused by physiological signals such as pulse waves.

Knee Motion: To evaluate the sensor's performance during large-scale body movements, it was attached to the knee and tested during walking and squatting. The resistance response during these activities is shown in Fig. 7. During walking, the sensor exhibited periodic

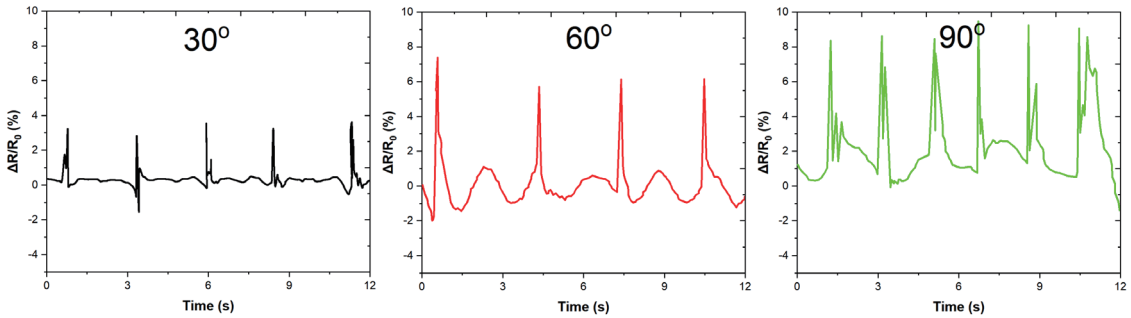

Fig. 5. (Color online) Relative resistance change ($\Delta R/R_0$) as a function of finger bending angle. Bending angles of 30, 60, and 90° resulted in relative resistance changes of 0.33, 0.78, and 0.92%, respectively.

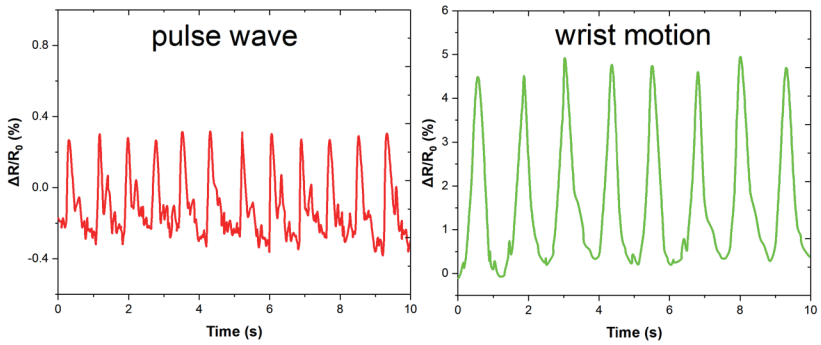

Fig. 6. (Color online) Relative resistance change ($\Delta R/R_0$) recorded during wrist motion. Pulse-wave monitoring detected periodic resistance changes corresponding to heartbeats, with an average relative change of 4.3%.

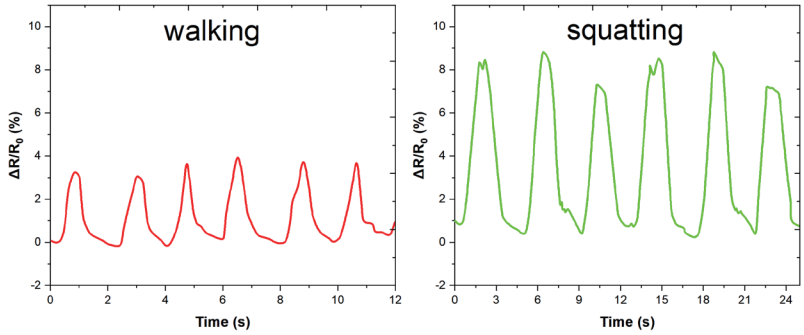

Fig. 7. (Color online) Strain sensor response during knee motion, including walking and squatting.

resistance changes with a peak-to-peak variation of 3.4%, corresponding to the cyclic stretching and relaxation of the knee joint. During squatting, the resistance increased by 4.7% at maximum knee flexion, demonstrating the sensor's ability to accommodate large strains without mechanical failure or signal degradation.

The results indicate that the strain sensor can reliably detect and quantify strain changes associated with various body motions. Its high sensitivity to small deformations, such as those caused by pulse waves, demonstrates its potential for physiological monitoring applications. Moreover, its ability to handle larger strains during activities such as squatting highlights its versatility for broader motion-tracking applications. The sensor's low hysteresis and stable performance over repeated cycles further underscore its suitability for wearable technologies. These findings suggest that the strain sensor can be effectively integrated into motion-tracking systems for applications in healthcare, sports, and human–machine interfaces. Furthermore, the sensor demonstrated excellent resistance stability under various temperature (20 to 40°C) and humidity (30 to 80%) conditions, confirming their robustness for practical wearable applications.

3.5 Comparison with existing technologies

To evaluate the performance of the developed strain sensor, a comparative analysis was conducted against previously reported wearable strain sensors in terms of sensitivity,

stretchability, and adhesion. The developed sensor exhibited a *GF* of 45 at a strain of 20%, which is higher than those of most reported sensors, such as graphene-based sensors (*GF* ≈ 30) and carbon nanotube (CNT)-based sensors (*GF* ≈ 25).[38,39] This enhanced sensitivity ensures the accurate detection of small strain changes, making it suitable for applications requiring precise motion tracking. Additionally, the stretchability of the sensor, measured as the maximum strain before mechanical failure, reached 120%, which is comparable to or exceeds the performance of other elastomer-based sensors. For instance, sensors based on PDMS/graphene composites typically exhibit stretchability around 100%, while CNT-based sensors generally fail at a strain of 80–90%.[40]

To provide a clearer and more systematic comparison, Table 3 has been added to benchmark the developed AgNW-based strain sensor against representative technologies reported in recent literature. The comparison includes *GF*, maximum strain, initial resistance, adhesion strategy, and key remarks for each technology. A key advantage of the proposed sensor is its conformal adhesion to various substrates, including human skin. Unlike sensors relying on adhesives or tapes, the elastomer encapsulation in this work provides intrinsic adhesion, which allows for secure attachment without additional adhesives. This property enhances user comfort and reduces the risk of delamination during prolonged use or repeated motion. Furthermore, the reusability of the sensor was demonstrated by maintaining over 95% of its initial sensitivity and adhesion strength after 50 attachment–detachment cycles, outperforming other sensors that often degrade after fewer cycles.

3.6 Long-term stability and reusability

The long-term stability and reusability of the developed strain sensor were evaluated through cyclic bending tests and repeated attachment–detachment cycles. These tests are critical to assess the durability and reliability of the sensor for practical wearable applications. The sensor was subjected to 100 bending cycles at a fixed angle of 60° to simulate repetitive motion. The resistance change during these cycles is shown in Fig. 8. The sensor exhibited consistent

Table 3
Benchmarking of strain sensors for large strain measurement.

Sensor type	*GF*	Max strain (%)	Initial resistance (Ω)	Adhesion method	Key remarks	Ref.
AgNW (This work)	45 (at 20% strain)	120	12.5 ± 1.2	Intrinsic elastomer adhesion (Ecoflex)	High sensitivity, low hysteresis, reusable	—
Graphene-based	~30	100	~50–100	Adhesive tape or epoxy	Moderate sensitivity, flexible but adhesion challenges	(38)
CNT-based	~25	80–90	~100–200	Adhesive or encapsulation	Good flexibility, low adhesion durability	(39)
Metal thin film (Au/Cr)	~5–10	<5	<10	Direct deposition	Low stretchability, high stiffness	(40)
Conductive polymer (PEDOT:PSS)	~20–30	60–80	~200–500	Encapsulation layer	Moderate sensitivity, poor long-term stability	(8)
MXene-based	~40	70–90	~30–80	Hydrogel encapsulation	High conductivity, water sensitivity	(7)

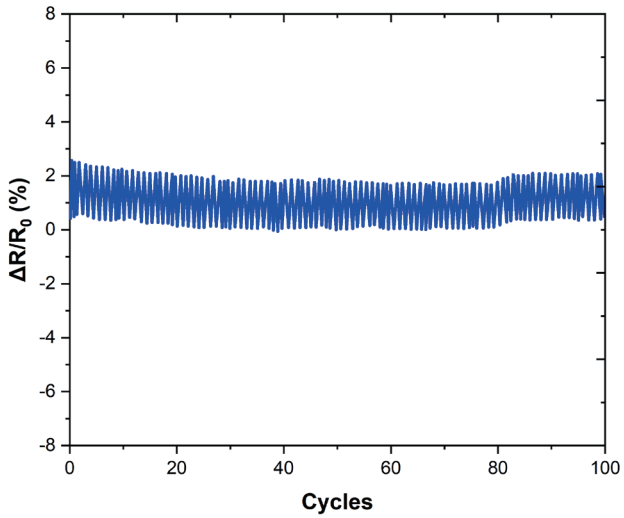

Fig. 8. (Color online) Relative resistance change ($\Delta R/R_0$) of the strain sensor over 100 bending cycles at a fixed bending angle of 60°.

resistance variations throughout the test, with less than 2% deviation in peak resistance after 100 cycles. This minimal drift indicates excellent mechanical and electrical stabilities under repeated strain. The sensor's robust performance can be attributed to the strong interfacial bonding between the conductive layer and the elastomer matrix, which prevents delamination or microcrack formation during deformation. Additionally, the sensor maintained fast response and recovery, with no notable lag or hysteresis, even after prolonged cycling.

To evaluate reusability, the sensor was detached and reattached to the skin 10 times, and the resistance signals were recorded during bending at each reattachment. Figure 9 shows the resistance response after each reattachment. The sensor consistently produced similar resistance signals, with less than 5% variation in sensitivity after 10 cycles. This performance demonstrates the sensor's ability to maintain stable adhesion and electrical properties despite repeated handling. The intrinsic adhesion provided by the elastomer encapsulation played a key role in ensuring conformal contact with the skin, reducing the risk of performance degradation due to misalignment or air gaps.

The results highlight the sensor's durability and reusability, which are critical for wearable applications requiring long-term operation and frequent repositioning. The ability to withstand 100 bending cycles with negligible signal degradation demonstrates its mechanical resilience and suitability for dynamic environments. Furthermore, the consistent performance after 10 attachment–detachment cycles underscores its potential for reusable and cost-effective wearable devices. These features position the developed sensor as a reliable and sustainable solution for motion tracking, physiological monitoring, and other wearable applications. While the developed strain sensor demonstrates high sensitivity, stretchability, and reusability, certain limitations need to be addressed to further enhance its performance and broaden its applicability.

One limitation of the current sensor is its maximum strain range, which is limited to 120%. While this stretchability is sufficient for most wearable applications, such as joint motion tracking and physiological monitoring, it may not be adequate for extreme strain conditions,

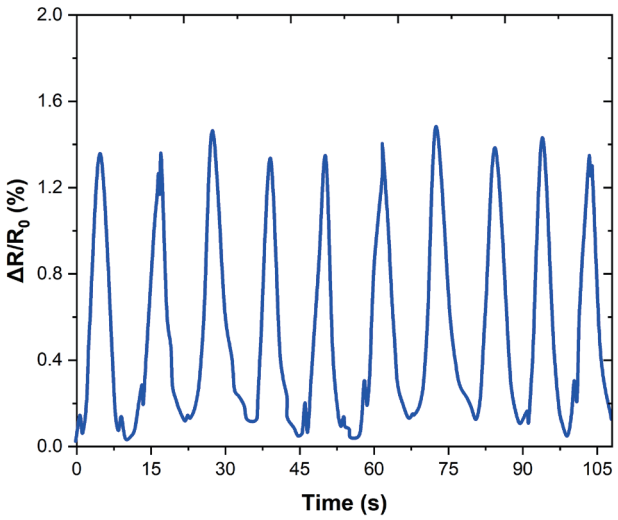

Fig. 9. (Color online) Relative resistance change ($\Delta R/R_0$) of the strain sensor recorded after 10 consecutive attachment–detachment cycles.

such as applications involving large-scale deformation in sports or robotics. Additionally, although the intrinsic elastomer-based adhesion provides conformal contact and stable performance over multiple attachment–detachment cycles, long-term adhesion under dynamic conditions (e.g., sweating or prolonged physical activity) remains a challenge. Extended exposure to moisture or oils from the skin may reduce adhesion strength and affect signal stability over time. Furthermore, the current design relies on wired connections for data acquisition, which may limit its practicality for real-time, untethered applications.

To address these limitations, several strategies can be explored. First, the use of alternative nanomaterials, such as hybrid nanocomposites combining graphene and silver nanowires, can enhance the sensor's mechanical robustness and extend its maximum strain range beyond 150%. These hybrid structures can also improve electrical conductivity, further increasing sensitivity. Second, incorporating surface treatments or bio-inspired adhesive designs, such as microstructured surfaces mimicking gecko feet, can improve long-term adhesion under dynamic and moist conditions. Third, integrating the sensor with wireless communication modules, such as Bluetooth or near-field communication, will enable real-time, untethered monitoring. This advancement will significantly enhance the sensor's usability in wearable health monitoring systems and Internet of Things applications*GF* quantifies RELATIVE ch. Finally, developing stretchable power sources, such as flexible batteries or energy-harvesting mechanisms, can further improve the sensor's independence and portability.

4. Conclusions

In this study, we successfully developed high-performance AgNW-based strain sensors with exceptional sensitivity, stretchability, and durability, demonstrating their potential for wearable applications. The sensors achieved a *GF* of 45 at a strain of 20% and a maximum stretchability

of 120%, outperforming many existing technologies such as graphene- and CNT-based sensors. The electrical properties were further quantified by calculating the sheet resistance (62.5 Ω/square) and resistance per unit length (0.625 Ω/mm), providing standardized metrics for comparison with existing strain sensing technologies. The multilayer encapsulation with Ecoflex provided superior adhesion (0.85 N/cm peel force) and durability, retaining an adhesion strength of 95% after 500 cycles at a strain of 20%. The sensors exhibited consistent resistance responses, with less than 2% drift over 100 bending cycles and stable performance after 10 attachment–detachment cycles. During motion tracking, the sensors reliably detected finger bending (resistance increased by 0.92% at 90°), wrist pulse signals, and knee movements, highlighting their versatility for healthcare and sports monitoring. The use of aerosol jet printing enabled precise AgNW deposition, achieving uniform networks with high electrical conductivity (initial resistance: 12.5 ± 1.2 Ω). These findings underscore the sensor's potential for real-time, reusable, and cost-effective wearable systems, while future work can address challenges in long-term adhesion and wireless integration to expand its applicability.

Acknowledgments

This work was supported by the Research and Practice of the "Three Knows" Teaching Method in College Track and Field Teaching Reform from the Perspective of Smart Teaching (HNJG-20231318) and Research on the High-Quality Development of College Physical Education Teaching Empowered by Artificial Intelligence under the Guidance of Practice (24C0547).

References

1 M. A. U. Khalid and S. H. Chang: Compos. Struct. **284** (2022) 115214. https://doi.org/10.1016/j.compstruct.2022.115214
2 H. Souri, H. Banerjee, A. Jusufi, N. Radacsi, A. A. Stokes, I. Park, M. Sitti, and M. Amjadi: Adv. Intell. Syst. **2** (2020) 2000039. https://doi.org/10.1002/aisy.202000039
3 H. Chen, F. Zhuo, J. Zhou, Y. Liu, J. Zhang, S. Dong, X. Liu, A. Elmarakbi, H. Duan, and Y. Fu: Chem. Eng. J. **464** (2023) 142576. https://doi.org/10.1016/j.cej.2023.142576
4 Y. Si, S. Chen, M. Li, S. Li, Y. Pei, and X. Guo: Adv. Intell. Syst. **4** (2022) 2100046. https://doi.org/10.1002/aisy.202100046
5 N. Afsarimanesh, A. Nag, S. Sarkar, G. S. Sabet, T. Han, and S. C. Mukhopadhyay: Sens. Actuators, A **315** (2020) 112355. https://doi.org/10.1016/j.sna.2020.112355
6 L. Tang, S. Wu, J. Qu, L. Gong, and J. Tang: Materials **13** (2020) 3947. https://doi.org/10.3390/ma13183947
7 Z. Shen, F. Liu, S. Huang, H. Wang, C. Yang, T. Hang, J. Tao, W. Xia, and X. Xie: Biosens. Bioelectron. **211** (2022) 114298. https://doi.org/10.1016/j.bios.2022.114298
8 J. J. Petronienė, A. Dzedzickis, I. Morkvėnaitė-Vilkončienė, and V. Bučinskas: Sens. Actuators, A **366** (2024) 114950. https://doi.org/10.1016/j.sna.2023.114950
9 B. Ji, X. Wang, Z. Liang, H. Zhang, Q. Xia, L. Xie, H. Yan, F. Sun, H. Feng, K. Tao, Q. Shen, and E. Yin: Int. J. Hum.-Comput. Interact. **40** (2024) 6793. https://doi.org/10.1080/10447318.2023.2212232
10 W. Zhu, S. Wang, Y. Lu, W. Yang, S. Ge, Z. Lou, S. He, S. Jiang, and J. Han: Ind. Crops Prod. **222** (2024) 119598. https://doi.org/10.1016/j.indcrop.2024.119598
11 D. Chen, Y. Cai, L. Cheng, S. Guo, T. Liu, S. Huang, H. Yu, Y. Wang, Z. Hu, and D. Gui: Measurement **225** (2024) 113992. https://doi.org/10.1016/j.measurement.2023.113992
12 F. Basarir, Z. Madani, and J. Vapaavuori: Adv. Mater. Interfaces **9** (2022), 2200866. https://doi.org/10.1002/admi.202200866
13 S. Raman and R. S. Arunagirinathan: Nanomaterials **12** (2022) 1932. https://doi.org/10.3390/nano12111932

14 L. Zhang, F. Jiang, L. Wang, Y. Feng, D. Yu, T. Yang, M. Wu, and M. Petru: Appl. Compos. Mater. **29** (2022) 1621. https://doi.org/10.1007/s10443-022-10029-0
15 D. Fu, R. Wang, Y. Wang, Q. Sun, C. Cheng, X. Guo, and R. Yang: Carbohydr. Polym. **283** (2022) 119135. https://doi.org/10.1016/j.carbpol.2022.119135
16 J. Feng, Y. Tian, S. Wang, M. Xiao, Z. Hui, C. Hang, W. W. Duley, and Y. N. Zhou: J. Mater. Sci. Technol. **84** (2021) 139. https://doi.org/10.1016/j.jmst.2020.12.060
17 H. Zhang, Y. Zhang, J. Zhang, X. Ye, Y. Li, and P. Wang: Polym. Compos. **42** (2021) 2523. https://doi.org/10.1002/pc.25997
18 R. Madhavan: J. Mater. Sci.; Mater. Electron. **33** (2022) 3465. https://doi.org/10.1007/s10854-021-07540-8
19 H. Du, Z. Fan, W. He, and J. Pan: Alexandria Eng. J. **82** (2023) 298. https://doi.org/10.1016/j.aej.2023.10.005
20 C. Chen, W. Luo, J. Xu, and D. Niu: Alexandria Eng. J. **80** (2023) 41. https://doi.org/10.1016/j.aej.2023.08.055
21 M. E. Barth, M. R. Pistore, F. A. Brehm, M. Mancio, and V. da L. de Souza: Matéria **29** (2024) e20230347. https://doi.org/10.1590/1517-7076-RMAT-2023-0347
22 B. J. Chen, Y. Liu, B. C. Liu, R. B. Huang, P. L. Wu, T. Jiang, X. Dong, X. Li, H. E. Khoo, and S. W. Lee: Matéria **29** (2024) e20230294.
23 W. Yang, C. Li, and L. Han: Carbon Lett. **35** (2024) 267. https://doi.org/10.1007/s42823-024-00788-0
24 Y. Jiang, Y. Chen, W. Wang, and D. Yu: Colloids Surf., A **639** (2021) 127477. https://doi.org/10.1016/j.colsurfa.2021.127477
25 Z. Yang, Z. Wu, D. Jiang, R. Wei, X. Mai, D. Pan, S. Vupputuri, L. Weng, N. Naik, and Z. Guo: J. Mater. Chem. C **9** (2021) 2752. https://doi.org/10.1039/D0TC04659K
26 H. Zhang, J. P. Choi, S. K. Moon,and T. H. Ngo: Addit. Manuf. **33** (2020) 101096. https://doi.org/10.1016/j.addma.2020.101096
27 Z. Li, S. Li, Y. Dai, and X. Peng: Appl. Opt. **49** (2010) 2947.
28 H. Jeong, J. H. Lee, S. Kim, S. Han, H. Moon, J.-Y. Song, and A.-Y. Park: Sci. Rep. **13** (2023) 21297. https://doi.org/10.1038/s41598-023-47544-4
29 Y. Zhang, D. Zhao, L. Cao, L. Fan, A. Lin, S. Wang, F. Gu, and A. Yu: Nanomaterials **13** (2023) 181. https://doi.org/10.3390/nano13010181
30 S. Agarwala, G. L. Goh, and W. Y. Yeong: IEEE Access **6** (2018) 63080.
31 B. Serbest, S. G. Kara, R. Alpay, T. Ataşer, B. Kınacı, N. Akın Sönmez, and S. Özçelik: J. Electron. Mater. **54** (2025) 1245. https://doi.org/10.1007/s11664-024-11615-7
32 X. Sui, J. R. Downing, M. C. Hersam, and J. Chen: Mater. Today **48** (2021) 135. https://doi.org/10.1016/j.mattod.2021.02.001
33 M. Tursunniyaz, A. Meredith, and J. Andrews: Sens. Actuators, A **364** (2023) 114777. https://doi.org/10.1016/j.sna.2023.114777
34 K. Jeong, Y. Lee, Y. Kim, H. Mun, K.-U. Kyung, and S. G. Im: Chem. Eng. J. **429** (2022) 132250. https://doi.org/10.1016/j.cej.2021.132250
35 Y. Kim, J. Kim, C. Y. Kim, T. Kim, C. Lee, K. Jeong, W. Jo, S. Yoo, T.-S. Kim, K. C. Choi, and S. G. Im: Chem. Eng. J. **431** (2022) 134074. https://doi.org/10.1016/j.cej.2021.134074
36 R. Xu, J. W. Lee, T. Pan, S. Ma, J. Wang, J. H. Han, Y. Ma, J. A. Rogers, and Y. Huang: Adv. Funct. Mater. **27** (2017) 1604545. https://doi.org/10.1002/adfm.201604545
37 H. Li, Y. Ma, and Y. Huang: Mater. Horiz. **8** (2021) 383. https://doi.org/10.1039/D0MH00483A
38 C. Parameswaran and D. Gupta: Nano Convergence **6** (2019) 28. https://doi.org/10.1186/s40580-019-0198-x
39 R. Herbert, J.-H. Kim, Y. S. Kim, H. M. Lee, and W.-H. Yeo: Materials **11** (2018) 187. https://doi.org/10.3390/ma11020187
40 S. Wu, S. Peng, and C. H. Wang: Sens. Actuators, A **279** (2018) 90. https://doi.org/10.1016/j.sna.2018.06.002